PNAS RESEARCH ARTICLE | BIOPHYSICS AND COMPUTATIONAL BIOLOGY OPEN ACCESS

A structure-based mechanism for initiation of AP-3 coated vesicle formation

Matthew Begley[a], Mahira Aragon[b], and Richard W. Baker[a,c,1]

Affiliations are included on p. 11.

Edited by James Hurley, University of California Berkeley, Berkeley, CA; received June 14, 2024; accepted October 14, 2024

Adaptor protein complex-3 (AP-3) mediates cargo sorting from endosomes to lysosomes and lysosome-related organelles. Recently, it was shown that AP-3 adopts a constitutively open conformation compared to the related AP-1 and AP-2 coat complexes, which are inactive until undergoing large conformational changes upon membrane recruitment. How AP-3 is regulated is therefore an open question. To understand the mechanism of AP-3 membrane recruitment and activation, we reconstituted human AP-3 and determined multiple structures in the soluble and membrane-bound states using electron cryo-microscopy. Similar to yeast AP-3, human AP-3 is in a constitutively open conformation. To reconstitute AP-3 activation by adenosine di-phosphate (ADP)-ribosylation factor 1 (Arf1), a small guanosine tri-phosphate (GTP)ase, we used lipid nanodiscs to build Arf1-AP-3 complexes on membranes and determined three structures showing the stepwise conformational changes required for formation of AP-3 coated vesicles. First, membrane recruitment is driven by one of two predicted Arf1 binding sites, which flexibly tethers AP-3 to the membrane. Second, cargo binding causes AP-3 to adopt a fixed position and rigidifies the complex, which stabilizes binding for a second Arf1 molecule. Finally, binding of the second Arf1 molecule provides the template for AP-3 dimerization, providing a glimpse into the first step of coat polymerization. We propose coat polymerization only occurs after cargo engagement, thereby linking cargo sorting with assembly of higher-order coat structures. Additionally, we provide evidence for two amphipathic helices in AP-3, suggesting that AP-3 contributes to membrane deformation during coat assembly. In total, these data provide evidence for the first stages of AP-3-mediated vesicle coat assembly.

endosome | vesicle coat | cargo sorting | AP-3

Significance

Cells control the spatial organization of their endomembrane network using multiple vesicular trafficking pathways. An ancient family of vesicle coats are the “adaptor protein” or AP complexes, which all descend from a common ancestor. While the functions of AP-1 and AP-2, which require clathrin, are relatively well understood, the clathrin-independent mechanisms of other AP complexes remain unclear. This study provides a structural mechanism for the recruitment and initial polymerization of AP-3, which mediates cargo sorting in tubular and recycling endosomes. Dimerization of AP-3 is mediated by the small guanosine tri-phosphate (GTP)ase Arf1 using the same interface that mediates Arf polymerization. We therefore propose that Arf1 and AP-3 collaborate to form clathrin-independent coats in the endosomal compartment.

Endosomes exist at the intersection of multiple trafficking pathways, including the secretory pathway, endocytosis, and regulated degradation through the lysosome (1). As many proteins traffic through the endosome as part of their normal function, while also being targeted for degradation at other times through endosome-dependent pathways, cells must be able to differentially select and sort cargo (2). An important component to maintaining the fidelity of this process is the recruitment of the adaptor protein (AP) coats AP-1 and (AP-3), which recognize and package cargo into coated vesicles (3). AP-1 and AP-3 are both regulated by adenosine di-phosphate (ADP)-ribosylation factor 1 (Arf1), small gunaosine tri-phosphate (GTP)ase and master regulator of membrane trafficking in multiple organelle compartments (4). As these coats segregate to distinct structures within the endosome and traffic a partially overlapping subset of cargo (5), how they are differentially controlled is an open question.

AP-1 and AP-3 are part of a larger family of vesicle coats (AP-1 through AP-5), which are structurally similar to the inner coat of COPI (6). AP complexes and coat protein complex I (COPI) all descend from an ancestral coat (7, 8), highlighting their structural and mechanistic conservation. All AP complexes have a shared domain organization: two large subunits, α/γ/δ/ε/ζ and β1-5, a medium subunit (μ1-5), and a small subunit (σ1-5) (*SI Appendix*, Fig. S1). Each of the large subunits also has an appendage domain connected to the central “core” via a flexible linker and which mediates binding to regulators and/or clathrin. The paradigm for AP function largely comes from our understanding of AP-1 and AP-2 (9) (*SI Appendix*, Fig. S1 *B* and *C*). When in the cytoplasm, both complexes exhibit a “closed” conformation where the C-terminal domain (CTD) of the μ-1/2 subunit tucks into the “bowl” of the core (10, 11). This closed form of the complex occludes the two known binding sites for transmembrane cargo: tyrosine-based YxxΦ motifs (where x is any amino acid and Φ is a bulky, hydrophobic amino acid) on the μ subunit (12, 13), and acidic dileucine-based motifs ([E/D]xxxL[L/I]) on the σ subunit (14). Both AP-1 and AP-2 recruit clathrin to form 30 to 50 nm coated vesicles. The largest distinction is that AP-1 is recruited and activated in the trans-Golgi network/endosome through Arf1 (15, 16), which also recruits COPI

Author contributions: M.B. and R.W.B. designed research; M.B., M.A., and R.W.B. performed research; M.B. contributed new reagents/analytic tools; M.B. and R.W.B. analyzed data; and M.B. and R.W.B. wrote the paper.

The authors declare no competing interest.

This article is a PNAS Direct Submission.

[1] To whom correspondence may be addressed. Email: baker@med.unc.edu.

This article contains supporting information online at https://www.pnas.org/lookup/suppl/doi:10.1073/pnas.2411974121/-/DCSupplemental.

in an analogous manner using conserved interfaces on the large subunits (17–19). In contrast, AP-2 is recruited and activated through its intrinsic affinity for the plasma-membrane enriched phosphatidylinositol 4,5 bisphosphate (PIP_2) (20). Thus, specificity in clathrin-mediated transport largely derives through regulated recruitment of AP-1/2 to distinct membranes.

In contrast, less is known about the molecular mechanisms of AP-3 regulation. For example, AP-3 has been reported to have both clathrin-dependent (21, 22) and -independent functions (23–25) and is found to only partially colocalize with clathrin in vivo (26, 27). More broadly, our structural understanding of AP-3 is largely derived from homology modeling with other AP complexes and a moderate-resolution electron cryo-microscopy (cryo-EM) structure from yeast AP-3 (28). Importantly, this study revealed that AP-3 is natively in an open conformation, in stark contrast to AP-1 and AP-2, which must be activated upon recruitment to the membrane (*SI Appendix*, Fig. S1*D*). The insight that AP-1 is natively closed (10) and AP-3 is natively open suggests that each complex has distinct pathways to forming vesicular and tubular coats. A recent report showed that AP-1 can polymerize on membrane tubules in an Arf1-dependent, clathrin-independent manner (29), suggesting that AP-1 acts to deform membranes and sort cargo into tubular assemblies before budding into clathrin-coated structures. However, a similar understanding of AP-3 function is hampered by a lack of structural and mechanistic information. As such, the molecular details that underpin the differential regulation of AP-1 and AP-3 are currently unknown.

To gain insight into the mechanism of AP-3 function and regulation, we developed a method for purification and reconstitution of human AP-3 and solved cryo-EM structures of the complex in the soluble and membrane-bound states. Using lipid nanodiscs to build membrane-bound AP-3 complexes, we determined multiple structures of Arf1- and cargo-bound AP-3. Our data show a stepwise conformational activation of the AP-3 complex that is unique from other AP complexes. AP-3 is conformationally flexible upon initial recruitment to the membrane yet is rigidified upon engagement with tyrosine cargo. Cargo binding precedes engagement with a second copy of Arf1, which "locks" the complex into a rigid conformation and templates initial dimerization of cargo-bound AP-3. We propose that the unique activation and coat assembly pathways for AP-1 and AP-3 are key to the differential function of these complexes in the same organelle compartment.

Results

Cryo-EM Structure of Human AP-3 in the Soluble State. To determine the structure of human AP-3, we developed a protocol for recombinant expression and purification in *E. coli*, similar to the protocols for purifying mammalian AP-1 (30) and AP-2 (11). After extensive optimization, we successfully purified the AP-3 core which lacks the appendages and unstructured linkers of the two large subunits (Fig. 1 *A* and *B*). To determine a cryo-EM structure of AP-3 core (hereafter simply referred to as AP-3), we prepared cryo-EM grids using traditional blotting and plunge freezing. Initial grids showed excellent two dimensional (2D)-class averages but with a strong preferred orientation (*SI Appendix*, Fig. S2*A*). To alleviate the preferred orientation problem, we used to a blot-free method for grid preparation (31), as this is documented to aid in grid preparation of samples known to adhere to the air–water interface (32). While these grids still had a noticeable preferred orientation problem, the increase in angular distribution and collection of multiple datasets at unique tilt angles resulted in a structure of soluble AP-3 at a nominal resolution of 3.6 Å (Table 1 and *SI Appendix*, Fig. S2 *B–E*).

AP-3 Natively Adopts an Open Conformation. Our cryo-EM data of soluble AP-3 shows an "open" structure (Fig. 1 *C–E*), similar to the reported conformation of yeast AP-3 (28), suggesting that the resting state of the complex is an evolutionarily conserved feature of AP-3. In this state, the CTD of the μ3 subunit has been ejected from the bowl formed by the two large subunits. In the case of AP-1 (10) and AP-2 (11), the μ1/2-CTD is firmly packed in the bowl, occluding cargo binding sites and holding the complex in an inactive conformation (*SI Appendix*, Fig. S1 *B* and *C*). While our structure is in an open conformation like yeast AP-3 (28), the μ3-CTD is not visible in our structure, suggesting that it does not adopt a fixed orientation in the soluble state (Fig. 1*F*).

A structural explanation for why AP-3 is natively open is unclear. Yeast AP-3 seems to be in an open state due to an insertion in the APL5/δ subunit, but this insertion is not conserved in humans (28) (*SI Appendix*, Fig. S3*A*). In the case of human AP-3, a possible explanation is the lack of a salt bridge which stabilizes the interface between the μ and γ/α subunits in AP-1 and AP-2, respectively (*SI Appendix*, Fig. S3 *B* and *C*). This salt bridge is conserved in AP-1 and AP-2 orthologs (*SI Appendix*, Fig. S3*D*), and, in the case of AP-2, an E302K mutation in the salt bridge causes the complex to become open without activation (33). AP-3 δ also contains a four-residue insert compared to AP-1 and AP-2, which causes a further steric clash preventing a closed conformation (*SI Appendix*, Fig. S3 *C* and *D*). Therefore, the basal open state of AP-3 is likely a conserved feature of the complex, although the mechanistic basis could potentially vary between species.

Arf1 Binds to AP-3 Primarily through the δ Subunit. AP-1 (15, 16, 34), AP-3 (21, 35), AP-4 (36), and COPI (17–19) have all been reported to be recruited to membranes through direct interaction with the small GTPase, Arf1. Through a multitude of structures and mutational analyses (29, 30), AP-1 has been shown to bind to Arf1 in two distinct locations—the γ and β1 subunits. Each interface interacts with Arf1 through the Switch I and II regions, explaining the GTP dependence of Arf1/AP-1 binding. Similarly, AP-3 is known to bind to Arf1, and crosslinking experiments have shown that it interacts with both the δ and β3 subunits (37). To determine the molecular details of these interactions, we purified guanosine di-phosphate (GDP)-locked (T31N) and GTP-deficient (Q71L) mutants of Arf1 as Halo-tag fusions and performed pull-down binding assays to compare binding of AP-3 hemicomplexes, full AP-3 complex, and full AP-1 complex in both the GDP and GTP-bound states (Fig. 2*A* and *SI Appendix*, Fig. S4*A*). Our data show that AP-3 binds robustly to Arf1 in a GTP-stimulated manner, with little background binding to a Halo-tag-only control (*SI Appendix*, Fig. S4*B*). Comparing the binding of AP-3 hemicomplexes, it is apparent that the δ-σ3 complex binds nearly as well as the full complex, with binding of the β3-μ3 hemicomplex barely above background levels in the $Arf1^{GTP}$ state. This suggests that the primary Arf1 binding site on AP-3 is on δ, in contrast to AP-1, which has been reported to interact more strongly with Arf1 through β1 (30).

Cryo-EM Structures of AP-3 on a Membrane. To determine the mechanism of AP-3 engagement with Arf1 and membranes, we reconstituted Arf1-AP-3 complexes on lipid nanodiscs (Fig. 2*B*) and solved their structure using single-particle cryo-EM (*SI Appendix*, Figs. S4–S7). We have previously shown that lipid nanodiscs are amenable to solving high-resolution structures of AP complexes and recapitulating known membrane-induced allostery (38). Briefly, we purified full-length, myristoylated Arf1-Q71L (hereafter *myr*Arf1) in *E. coli* and verified the lipidation using mass spectrometry (*SI Appendix*, Fig. S4 *C* and *D*) and through guanine-nucleotide exchange factor (GEF)-mediated loading onto

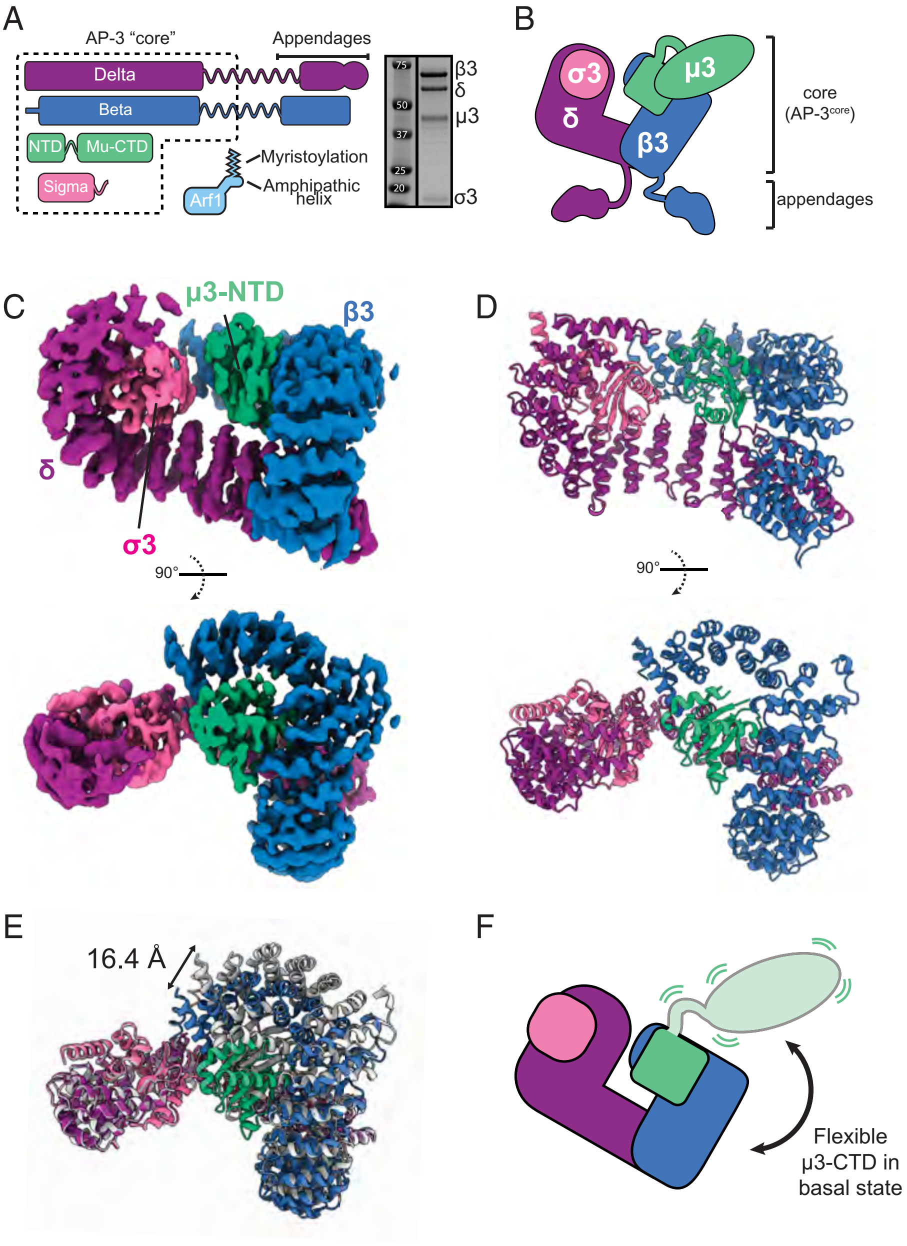

Fig. 1. AP-3 is in a basal open state. (*A*) Domain schematic for human AP-3 and strategy for recombinant purification. A representative sodium dodecyl sulfate–polyacrylamide gel electrophoresis (SDS-PAGE) gel is shown. (*B*) Cartoon representation of AP-3, showing the core and the appendages. (*C*) Cryo-EM density for soluble AP-3 core, colored by subunit. (*D*) Associated molecular model for cryo-EM structure shown in *C*. (*E*) Structural alignment of the two most divergent three dimensional (3D) classes from the soluble AP-3 cryo-EM processing. Models were aligned using σ3. Resolution for the maps was 3.83 Å (colored model) and 5.08 Å (gray model). (*F*) Model for conformational flexibility within soluble AP-3, showing that the µ3-CTD is not in a fixed location and is flexibly tethered to the complex.

MSP2N2 nanodiscs (*SI Appendix*, Fig. S4*E*). To form Arf1-AP-3 complexes, we incubated AP-3 on 5% PI(3)P enriched nanodiscs containing a synthetic oleic-acid conjugated cargo peptide, followed by addition of *myr*Arf1, GTP, and a truncated form of the GEF, ARNO, which promotes the exchange of GDP for GTP by Arf1 (Fig. 2*B* and *SI Appendix*, Fig. S4*F*). To select the ideal cargo for structural analysis, we performed a pull-down assay with a panel of Halo-tagged cargo motifs from a variety of known trans-membrane cargoes (*SI Appendix*, Fig. S4*G*). From this panel of cargoes, CD63 and lysosomal-associated membrane protein 1 (LAMP1) pull down the most AP-3, suggesting they have the highest intrinsic affinity for AP-3, without membrane or Arf1 present. Cryo-EM grids containing the AP-3/Arf1/LAMP1-nanodisc complex were prepared using blot-free methods and single-particle data were collected on a 300-keV Titan Krios cryoTEM.

Data processing revealed a mix of three predominant species: 1) AP-3 complexes bound to a single copy of Arf1 on the δ subunit, with no density for µ3-CTD or bound cargo; 2) AP-3 bound to two copies of Arf1, with the µ3-CTD in a fixed position and bound to LAMP1; and 3) a dimer of the double-Arf1-cargo-AP-3 complex (Table 1 and *SI Appendix*, Figs. S5–S7). We refer to these structures as AP-3$^{\text{monoARF}}$, AP-3$^{\text{ARF+cargo}}$, and AP-3$^{\beta\text{-dimer}}$, respectively. The mechanistic details of these structures and the implications for a stepwise recruitment and assembly pathway to build activated AP-3 complexes are discussed below.

Cryo-EM Structure of AP-3 Bound to a Single Arf1 Molecule. After extensive 2D- and 3D-classification of our LAMP1-nanodisc data, we obtained a cryo-EM reconstruction of the AP-3$^{\text{monoARF}}$ complex with a nominal resolution of 4.7 Å. In this complex (Fig. 2 *C* and *D*), the µ3-CTD is not in a fixed orientation, which was also observed in the structure of soluble AP-3. Indeed, the overall conformation of AP-3 in the soluble and mono-Arf1-bound states is nearly identical (Fig. 2*E*). As no µ3-CTD is observed in this complex, it is likely that AP-3 is not bound to cargo peptide and this state represents the initial engagement of AP-3 with the membrane via the δ-Arf1 interface (Fig. 2*F*). We also do not observe density for the lipid bilayer of the nanodisc, presumably because Arf1 is flexibly tethered to the membrane (39) and AP-3 has low intrinsic affinity for membranes (28).

Table 1. Cryo-EM statistics

	apo AP-3	AP-3 monoArf1	AP3 Arf1+cargo	AP-3 dimer	Beta-Arf1 dimer
EMPIAR ID	EMPIAR-12310	EMPIAR-12311	EMPIAR-12311	EMPIAR-12311	EMPIAR-12311
EMDB ID	EMD-45214	EMD-45207	EMD-45210 (Consensus Map) EMD-45211 (Focus Map 1) EMD-45212 (Focus Map 1) EMD-4513 (Combined Map)	EMD-45208	EMD-45209
PDB ID	9C5C	9C58	9C5B	9C59	9C5A
Data Collection					
Microscope	Titan Krios	Titan Krios	Titan Krios	Titan Krios	Titan Krios
Camera	Gatan K3 (super-res)	Gatan K3 (counting)	Gatan K3 (counting)	Gatan K3 (counting)	Gatan K3 (counting)
Magnification	105,000×	81,000×	81,000×	81,000×	81,000×
Voltage (kV)	300	300	300	300	300
Dose rate (e^-/pixel/s)	29.1	26.7	26.7	26.7	26.7
Exposure time (s)	1.72	2	2	2	2
Number of frames	50	50	50	50	50
Total electron exposure (e^-/Å2)	50	53.4	53.4	53.4	53.4
Defocus range (μm)	0.4 to 1.4	0.4 to 1.4	0.4 to 1.4	0.4 to 1.4	0.4 to 1.4
Pixel size (Å)	0.413	1.058	1.058	1.058	1.058
Number of micrographs	17,545	11,601	6,108	6,108	6,108
Reconstruction					
Image processing package	cryoSPARC	cryoSPARC	cryoSPARC	cryoSPARC	cryoSPARC
Final particle images (no.)	1,205,158	285,082	176,749	122,155	122,155
Symmetry imposed	*C1*	*C1*	*C1*	*C2*	*C2*
Map resolution (Å)	3.6	4.7	4.5	4.3	4.2
FSC threshold	0.143	0.143	0.143	0.143	0.143
Map resolution range (Å)	3.0 to 10	4.1 to 10	3.9 to 12	4.8 to 11	3.6 to 12
Map sharpening B-factor ($Å^2$)	−193	−317	−177	−179	−156
Model Refinement					
Refinement package	Rosetta, Phenix	Rosetta, Phenix	Rosetta, Phenix	Rosetta, Phenix	Rosetta, Phenix
Model composition					
Nonhydrogen atoms	11,364	7,954	16,879	33,740	16,338
Protein residues	1,429	1,590	2,114	4,226	2,046
Ligands	0	1	4 (GTP: 2, MG:2)	8 (GTP: 4, MG 4)	4 (GTP: 2, MG:2)
B factors (Å2); min/max/mean					
Protein	14.3/129.3/60.4	96.7/367.4/191.4	30.0/343.33/178.97	66.78/380.03/166.7	50.5/297.0/128.0
Ligand	–	216.3/242.6/242.0	118.2/258.6/196.9	118.2/258.6/196.9	90.50/91.9/90.9
rmsd					
Bond lengths (Å)	0.005	0.005	0.013	0.005	0.014
Bond angles (°)	1.048	1.129	1.258	1.044	1.358
MapCC (volume/mask)	0.63/0.66	0.62/0.63	0.77/0.77	0.70/0.71	0.78/0.79
Validation					
MolProbity score	1.93	1.05	1.34	1.91	1.54
Clash score	20.16	1.47	5.15	19.55	5.00
Poor rotamers (%)	0.08	0	0.11	0.16	0.55
Ramachandran Plot					
Favored (%)	97.32	97.09	97.71	97.4	95.95
Allowed (%)	2.68	2.91	2.1	2.6	3.71
Outliers (%)	0	0	0.19	0	0.34

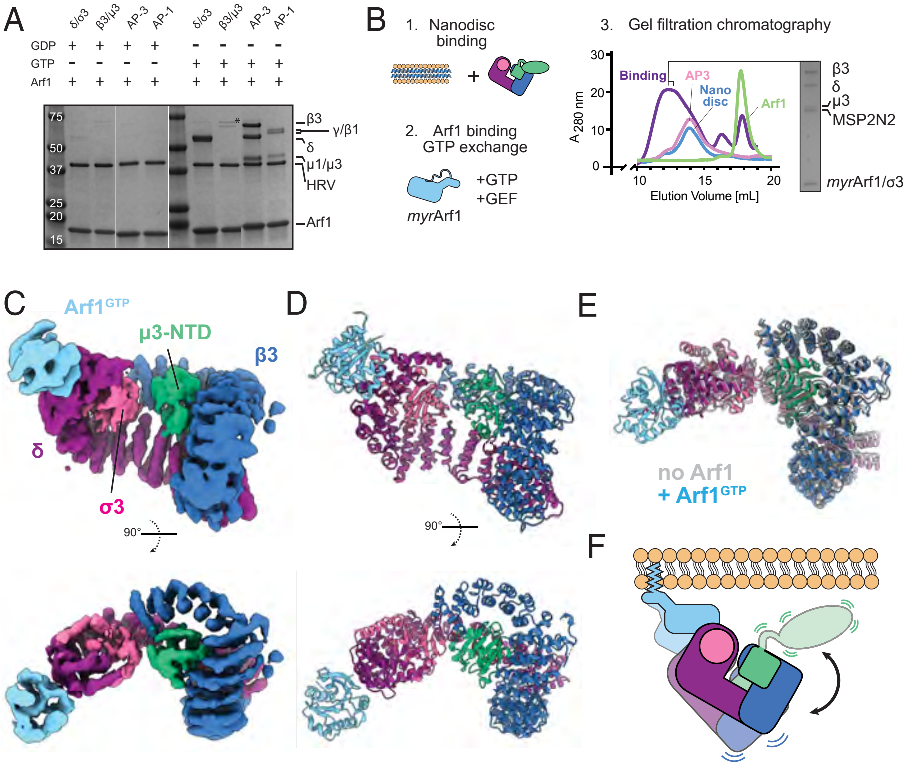

Fig. 2. AP-3 is recruited to membranes via an Arf1-delta (δ) interaction. (*A*) Pull-down assay between Halo-tagged Arf1 and AP-1, AP-3, and AP-3 hemicomplexes. Samples are eluted on the beads using an HRV protease site between Arf1 and the Halo tag. GDP conditions used an Arf1 T31N mutant, which is GDP locked. GTP conditions used an Arf1 Q71L mutant, which is hydrolysis deficient. GDP/GTP exchange was performed during initial binding to the resin. The asterisk denotes a contaminant in the β3-μ3 purification. Gel is Coomassie stained. (*B*) Schematic for assembly of Arf1-AP-3 nanodiscs, with a gel filtration binding assay showing complex assembly. (*C*) Cryo-EM structure of AP-3 bound to Arf1 on a lipid nanodisc. (*D*) Molecular model for AP-3 bound to a single molecule of Arf1 (AP-3^{monoArf1}). (*E*) Comparison of soluble AP-3 and AP-3^{monoArf1} complexes. Models were aligned using σ3. (*F*) Schematic for the conformational dynamics of AP-3 bound to Arf1 on a membrane. Note: All gels shown are Coomassie stained.

In this structure, Arf1 is bound at the δ interface, with clear secondary structure to unambiguously dock Arf1 with its Switch I and II regions binding to helices 4 and 6 of δ (*SI Appendix*, Fig. S8*A*). The overall orientation of Arf1 is nearly identical to the analogous binding site for AP-1 γ and COPI (18), with the most important interface residues being conserved between the complexes (*SI Appendix*, Fig. S8*B*). Mutation of conserved interface residues in δ reduced binding to Arf1 in a pull-down assay (*SI Appendix*, Fig. S8*C*), as shown for AP-1 (30). The most striking difference between AP-1 and AP-3 in the Arf1-activated state is the primary use of the δ interface for AP-3 versus the β1 interface for Arf1, which mirrors the results of our pull-down assay (Fig. 2*A*).

Cryo-EM Structure of Cargo-Bound AP-3 with Two Arf1 Molecules. In addition to AP-3 bound to a single Arf1 molecule, our LAMP1-nanodisc dataset showed a subset of particles with clear density for a second molecule of Arf1 along with the μ3-CTD, with additional particles showing dimers of this cargo-bound complex. The conformation of the AP-3 protomer in the monomeric and dimeric forms was nearly identical (rmsd of 1.55 Å), so we used signal subtraction and symmetry expansion to combine all particles into a single refinement of monomeric, cargo-bound AP-3. This analysis led to a model with a nominal resolution of 4.5 Å, sufficient to unambiguously dock all components and build an all-atom model using AlphaFold2 and Rosetta. We term this the AP-$3^{\mathrm{ARF+cargo}}$ complex.

In this structure, AP-3 is bound to two copies of Arf1 (Fig. 3*A*). The Arf1 molecule bound to δ is identical to that observed for the mono-Arf1 structure, showing that major structural rearrangements of this interface do not occur. The β Arf1 molecule is bound at the predicted interface based on the binding of Arf1 to AP-1 and COPI (*SI Appendix*, Fig. S8*D*). Mutation of conserved interface residues in β3 reduced binding to Arf1 in a pull-down assay (*SI Appendix*, Fig. S8*C*), as shown for AP-1 (30).

In addition to a second copy of Arf1, we also observe a fixed location for the μ3-CTD, packed against the surface of the β3 subunit. This general binding site for the μ-CTD is structurally conserved between AP-1 (30), AP-2 (40), and AP-3 (28). There is also clear density for the LAMP1 cargo motif in the μ3-CTD tyrosine cargo-binding pocket, unambiguously showing that this complex represents the cargo-engaged state of AP-3 (Fig. 3*B*). Surprisingly, the dileucine cargo-binding site on σ3 is occupied by the N-terminal extension of β3 (Fig. 3*C*), in addition to the β3 subunit being overall more rigid and in a more compact orientation compared to AP-3^{monoARF} (*SI Appendix*, Fig. S9*A*). AP-1 and AP-2 both have short N-terminal extensions on their β subunits, which pack into the dileucine cargo-binding pocket on σ in the closed conformation (Fig. 3*C*). Activation of both complexes leads to disruption of this interaction, as packing into the dileucine pocket is not observed in any of the reported open AP-1 or AP-2 structures (*SI Appendix*, Fig. S9*B*). Observation of β3 packing into the dileucine binding pocket in the presence of tyrosine cargo suggests that the two cargo binding sites are potentially linked through a series of conformational changes upon cargo and Arf1 binding. Alternatively, this structure may represent a partially activated state, whereby full activation requires ejection on the β3 tail, potentially by engagement of a dileucine cargo motif.

We next compared our AP-$3^{\mathrm{ARF+cargo}}$ structure to the cargo-bound conformations of AP-1 and AP-2 (Fig. 3 *D* and *E*). This analysis shows that each complex adopts a unique structure and that the membrane binding surfaces are related, but distinct. In the case of AP-1, the μ1-CTD reaches across the cleft of the bowl to interact with the Arf1-γ interface, with the γ-β1 interface splayed apart. An important consideration is that all available AP-1 structures with tyrosine cargo also contain a bound dileucine cargo (29, 41, 42). Conversely, the μ3-CTD of AP-3 does not make contact with δ or the δ-bound Arf1. Instead, packing of β3 into the σ3 dileucine cargo-binding pocket keeps the μ3-CTD distal from the Arf1-δ interface. AP-2 exists in an intermediate conformation, where neither the β2 nor μ2-CTD is contacting the α subunit. An overlay of AP-3 (green) with the μ1-CTD (pink) and μ2-CTD (blue) shows the different orientation of this subunit between the three complexes (Fig. 3*E*). Overall, cargo-binding promotes a unique conformation for AP-3 compared to other AP

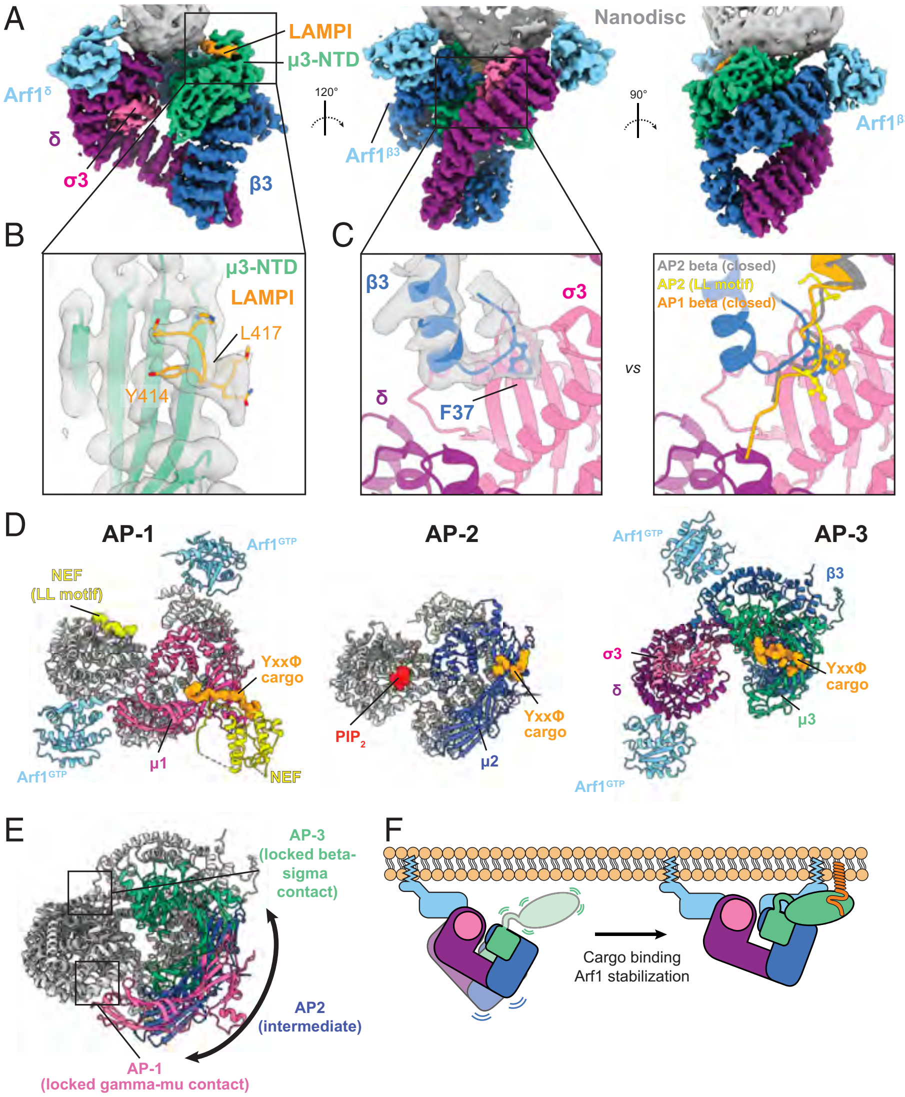

Fig. 3. Cryo-EM structure of the activated AP-3$^{ARF+cargo}$ supercomplex. (*A*) Cryo-EM structure of AP-3 bound to Arf1 and LAMP1 cargo peptide on a lipid nanodisc. (*B*) Zoomed in view of the AP-3-LAMP1 cargo binding interface. (*C*) Zoomed in view of the β3 tail packing into the dileucine binding pocket, compared with the same view of the closed AP-1 (orange) and AP-2 structures (gray) and AP-2 bound to the CD4 dileucine cargo motif (yellow). (*D*) Comparison of the cargo-bound AP-1 (7UX3.pdb), AP-2 (8T1O.pdb), and AP-3 complexes. Alignment was done using σ1, σ2, and σ3. (*E*) Overlay of cargo-bound AP-1, AP-2, and AP-3 complexes aligned as in *D*. All subunits are colored gray except the µ1/2/3-CTDs to emphasize the conformational changes between the three complexes. (*F*) Schematic for stabilization of AP-3 upon cargo binding, leading to recruitment of a second Arf1 molecule.

complexes that stabilizes and rigidifies the membrane-bound conformation (Fig. 3*F*).

Cryo-EM Structure of an Arf1/AP-3 Dimer. Unexpectedly, within our LAMP1-nanodisc data, we also observed a small number of particles that have two copies of AP-3, each bound to two copies of Arf1 and a LAMP1 YxxΦ-cargo peptide. These particles are overall much better behaved and with improved B-factors and angular distribution, leading to a 4.3 Å reconstruction. (Fig. 4*A*) The complex exhibits C2-symmetry, albeit with a rather flexible orientation along the symmetry axis. We refer to this complex as AP-3$^{β\text{-dimer}}$. Each AP-3/Arf1/cargo protomer in the AP-3$^{β\text{-dimer}}$ is very similar to the monomeric AP-3$^{ARF+cargo}$ complex. The dimer interface is largely mediated by Arf1 molecules on each β3 subunit forming a symmetrical contact (Fig. 4 *A* and *B*). Amorphous density corresponding to the nanodisc membrane is observed between the two AP-3 protomers, with all known membrane binding surfaces juxtaposed to this density.

While AP-2 has not been shown to multimerize, AP-1 is able to tubulate cargo-containing membranes in the presence of the HIV hijacking protein Nef (29). In these structures, several interfaces for AP-1 multimerization are observed, depending on the diameter of the tubule analyzed, suggesting structural plasticity in the formation of coated assemblies as they form and mature. Our AP-3 dimer interface does not match well with any analogous AP-1 interfaces, suggesting that the ultrastructure of the AP-1 and AP-3 coats are distinct. The most comparable AP-1 dimer utilizes two copies of Arf1 at a β1–β1 interface, but this contact also has a strong contribution from the µ1-CTDs and the Arf1 molecules are not making contact (Fig. 4 *B*, *Left*). In the case of AP-3, the interface is primarily driven by the Arf1 molecules themselves (Fig. 4 *B*, *Right*).

Within the polymerized AP-1 lattice are also two homodimeric Arf1 interfaces that mediate contact between adjoining AP-1 protomers. One Arf1-dimer mediates a γ–γ interface, while the other is part of a larger interface between four copies of β1 (*SI Appendix*, Fig. S10*A*). These Arf1 dimeric interfaces are nearly identical to one another. Comparatively, the Arf1–Arf1 homodimer seen in our AP-3 structure uses a distinct interface from that in AP-1 assemblies (Fig. 4*C*). Whereas the AP-1-Arf1 homodimers use a primarily charged interface (D114, R117, H150, R149), the AP-3 Arf1 homodimer is mostly apolar (Y35, L39, I42, V43, T44). The best analog for this dimeric interface is the primary oligomerization interface used by Arf6, as seen in a helical reconstruction of Arf6 polymers on a membrane (43) (*SI Appendix*, Fig. S10 *B* and *C*). This interface is conserved in Arf1, and previous studies have suggested a dimer of Arf1 is responsible for membrane deformation and vesicle scission (44, 45). This proposed dimer was disrupted by mutation of Arf1 Y35 (45), which mediates both the primary interface of the Arf6 helical polymer (43) and the

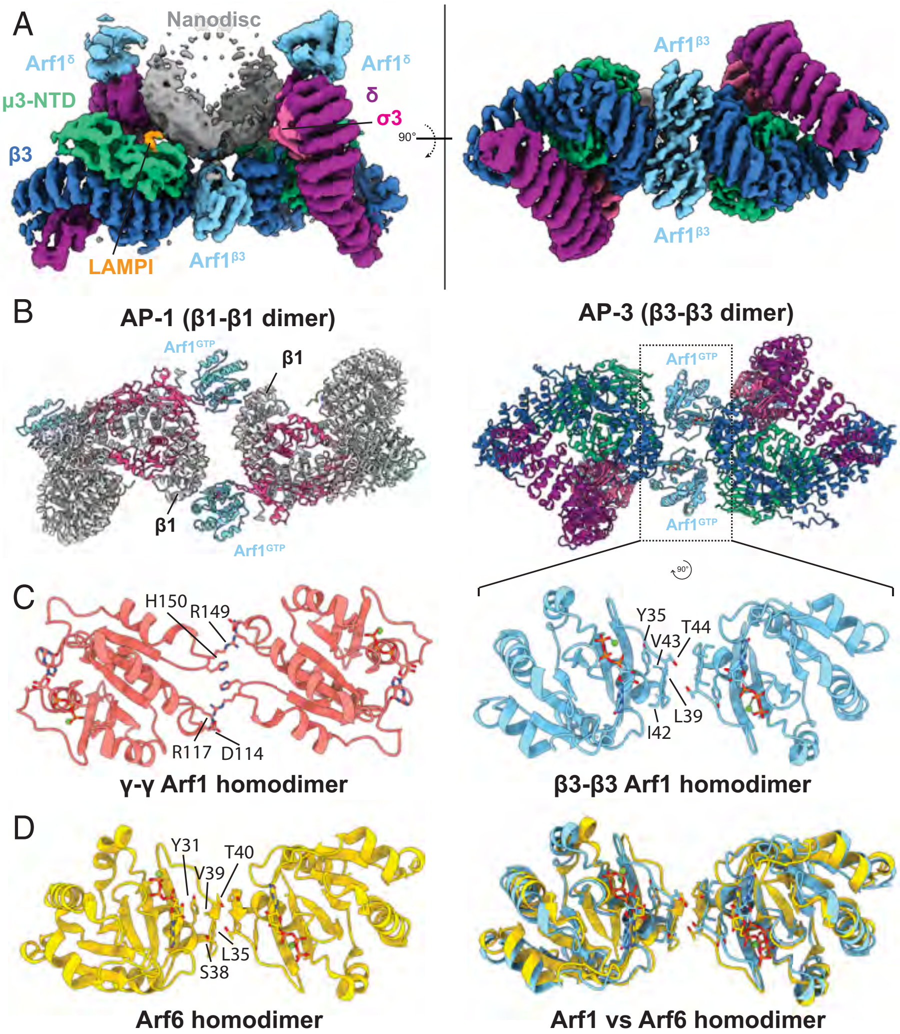

Fig. 4. Cryo-EM structure of the cargo-bound AP-3 dimer. (*A*) Cryo-EM density for the AP-3 dimer complex on a lipid nanodisc. Each protomer is bound to two Arf1 molecules and a LAMP1 cargo peptide. (*B*) Zoom-in view of the Arf1–Arf1 homodimer that mediates AP-1 and AP-3 dimerization. (*C*) Comparsion of an Arf1 homodimer (8D9V.pdb) within AP-1 tubules with the Arf1 homodimer observed in nanodisc-bound AP-3. (*D*) Comparison of the Arf6 homodimer observed on tubulated membranes (7XRD.pdb; chains A, B) with the Arf1 homodimer observed in nanodisc-bound AP-3.

AP-3-Arf1 dimer from this study (Fig. 4 *C* and *D*). Therefore, AP-3 seems to be co-opting an ancestral function of Arfs to polymerize and potentially tubulate membranes to build a lattice for adaptin-mediated cargo sorting. As we only observe Arf1 bound to the β subunit when also bound to YxxΦ-cargo, we propose a model for coat polymerization that requires AP-3 to first engage with cargo, rigidifying β3 and recruiting a second copy of Arf1, subsequently providing an interface for initial polymerization.

AP-3 Likely Engages with Curved Membranes. While the AP-3$^{\beta\text{-dimer}}$ is unambiguously engaged with a membrane, the overall structure is not compatible with binding to a flat membrane (*SI Appendix*, Fig. S11 *A* and *B*). Indeed, the AP-3$^{\beta\text{-dimer}}$ appears to be bound to the side of the nanodisc, making symmetric contacts with both "faces" of the disk as well as the MSP2N2 scaffolding. This suggests that our dimeric assembly best represents AP-3 assemblies bound to a curved membrane, such as a tubule. However, our AP-3$^{\beta\text{-dimer}}$ structure would require an extremely constricted membrane tubule between 6 and 7 nm (*SI Appendix*, Fig. S11*C*), representing the very latest stages of membrane thinning and deformation during vesicle budding. As membrane-deforming polymers must necessarily undergo structural rearrangements as the membrane bends and constricts, we reasoned that we could use observed structural plasticity in AP-3 to model other conformations of AP-3 that could bind to membranes of different curvature. Our processing of soluble AP-3 showed an ~10° flexing between the most divergent 3D classes (Fig. 1*E*), and yeast AP-3 was solved in three unique conformations with upward of 50° of torsion in the complex (28). We therefore used our AP-3$^{\beta\text{-dimer}}$ structure as a template to model dimeric structures of yeast AP-3 in the compact, intermediate, and stretched conformations, and manually docked them against a 10-nm membrane tubule (*SI Appendix*, Fig. S11*C*). While the compact AP-3 conformation is too constricted for binding to a 10 nm tubule, the intermediate conformation perfectly places all Arf1 amphipathic helices (AH) in the outer leaflet of the bilayer. The stretched conformation represents more shallow curvature, corresponding to an ~14 nm tubule. This suggests that simple flexing in the core of AP-3 would accommodate a variety of membrane curvatures that would be experienced as coat assembly proceeds from a flat to a highly curved assembly.

Assembly of AP-3 polymers on membrane tubules will necessarily require further polymerization beyond what is observed in our nanodisc data. As the observed conformation in the AP-3$^{\beta\text{-dimer}}$ is a head to head binding at β3, polymerization would require a δ–δ interface, much like AP-1 requires both β1–β1 and γ–γ contacts to build a helical lattice (29). While our nanodisc cryo-EM data did not capture any AP-3 dimers mediated by a δ–δ interface, we did observe a small population of 2D class averages in the soluble AP-3 data that clearly represent dimers mediated by a δ–δ interface (*SI Appendix*, Fig. S11 *D*–*F*). This interaction was observed in the absence of Arf1, yet it is reminiscent of the AP-1 γ–γ interface, which has direct contact between γ–γ, with Arf1 at the edges of the interface (*SI Appendix*, Fig. S10*A*). The details of

AP-3 polymerization on membranes remain to be fully described, but these data support a model of AP-3 assembly beyond the β3–Arf1 dimeric interface.

AP-3 Contains Two AH Domains that Bind Membranes. For each of our AP-3 structures, we began model building by docking in AlphaFold2-multimer predictions of all subunits and removing regions that were not accounted for in the density. While most regions of the prediction matched the expected domain organization of AP complexes, two regions of AP-3 were notable when building the AP-3$^{\beta\text{-dimer}}$ structure. First, the N terminus of δ has a short extension that is predicted to be helical by AlphaFold2. Second, a short region of the μ3 linker is also predicted to be helical by AlphaFold2. While the N-terminal helix of δ is in an analogous membrane-binding region of other AP complexes, the μ3 linker helix was notable for its unexpected juxtaposition to the membrane in our structure (Fig. 5*A*). Surprisingly, both of these helices from the AlphaFold2 prediction are close to unassigned cryo-EM density that is clearly in the plane of the membrane. Based on primary sequence, they both appear to be amphipathic helices (AH) (Fig. 5*B*) and we therefore built them into the cryo-EM density as membrane-inserting helices.

We performed a bioinformatic analysis to see whether these predicted helices were amphipathic in nature and judged their conservation. Using the HeliQuest tool (46), we analyzed the putative δ and μ3 AH domains. Both helices follow a heptad-repeat sequence, have a clear hydrophobic face, and have a high predicted hydrophobic moment, all of which are common features of AH domains. Using AlphaFold2 predictions to do a structural alignment of other AP complexes, only AP-3 δ and AP-4 ε have potential AH domains (*SI Appendix*, Fig. S12 *A* and *B*). When comparing AP-3 orthologs, while the primary sequence of the δ amphipathic helix is not well conserved, the helical nature and the heptad repeat structure are conserved (Fig. 5*B* and *SI Appendix*, Fig. S12*C*). A similar level of domain conservation without sequence conservation is observed for the μ3-linker helix (Fig. 5*B* and *SI Appendix*, Fig. S12*D*). It should also be noted that while AP-1 and AP-2 contain helices in their μ-linkers, these pack against the β subunit, and are further regulated by phosphorylation (47).

To test whether these helical domains bind to membranes, we purified each AH domain as an mGreenLantern (mGL)-fusion and performed membrane binding assays, similar to previous studies (48). We coated silica microspheres with membranes to create supported lipid bilayers (SLBs) and performed pelleting assays. Compared to the mGL control, both of the AH fusions robustly bound to SLBs (Fig. 5*C*). To test the mechanism of membrane insertion, we compared binding after washing in 1 M salt or 0.1% Triton. While the 1 M salt wash did not abrogate binding, each AH domain was washed away with 0.1% Triton. As a control, we simultaneously tested binding of *myr*Arf1, which is known to insert into membranes, and has an exceptionally strong AH domain (49). While *myr*Arf1 was resistant to high salt washing, it was removed with 0.1% Triton. Therefore, the predicted AH domains of AP-3 bind to the membrane and insert into the bilayer like traditional AH domains (Fig. 5*D*), raising the possibility that AP-3 contributes to membrane deformation like other vesicle-associated proteins that contain AH domains (50).

Discussion

This work provides a structure-based mechanism for the initial recruitment and activation of the AP-3 vesicle coat complex. We determined cryo-EM structures of AP-3 in four distinct states, which provide a clear structural framework for understanding the stepwise assembly of AP-3 into larger coat assemblies that are laden with trans-membrane cargo (Fig. 6). Our data show that the natively open state of AP-3 is conserved across species and build on these findings to show how AP-3 is recruited to membranes via two distinct Arf1 binding sites. The β3–Arf1 binding site is only observed when AP-3 is bound to YxxΦ cargo, suggesting that the flexible nature of the complex is stabilized upon cargo capture.

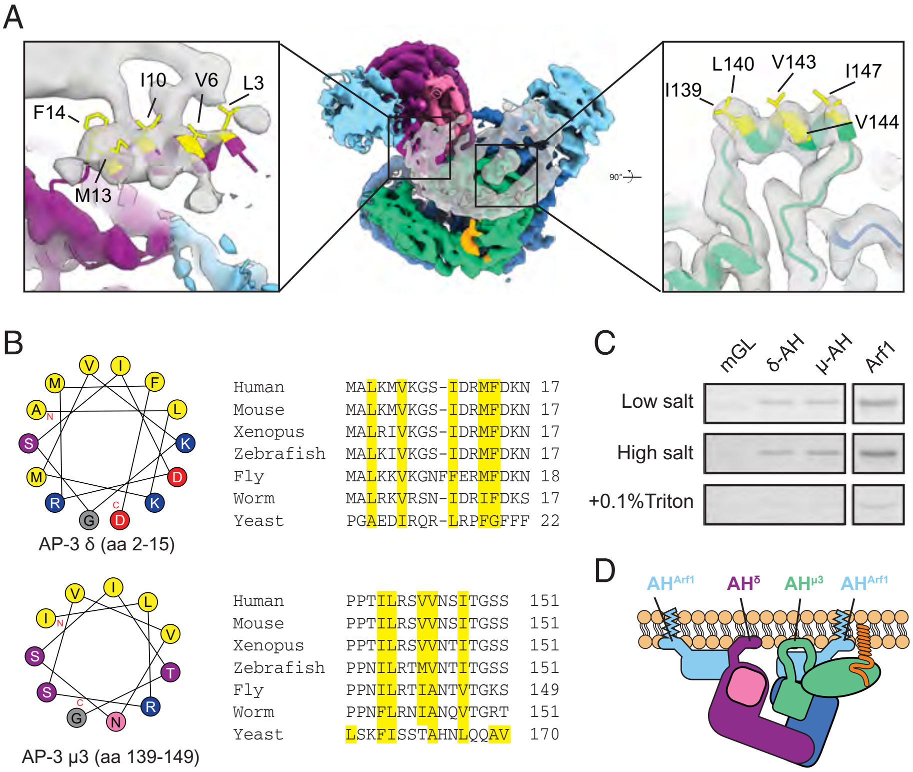

Fig. 5. AP-3 contains two AH domains. (*A*) Cryo-EM model of AP-3$^{\text{ARF+cargo}}$ (*Center*) with a zoom-in view of cryo-EM density for an amphipathic helix on the δ (*Left*) and μ3 subunits (*Right*). (*B*) Helical wheel diagrams and sequence alignments for the δ and μ3 AH. The hydrophobic face for each helix is colored yellow in the schematic and the alignments. (*C*) Membrane binding assay for mGreenLantern (mGL) fusions of the δ and μ3 AH. For each construct, binding was done identically and then washed with either low salt (LS, 100 mM NaCl), high salt (HS, 1 M NaCl), or 0.1% Triton X-100 buffers. Gel is Coomassie stained. (*D*) Schematic of membrane-bound AP-3 showing all known and predicted AH domains.

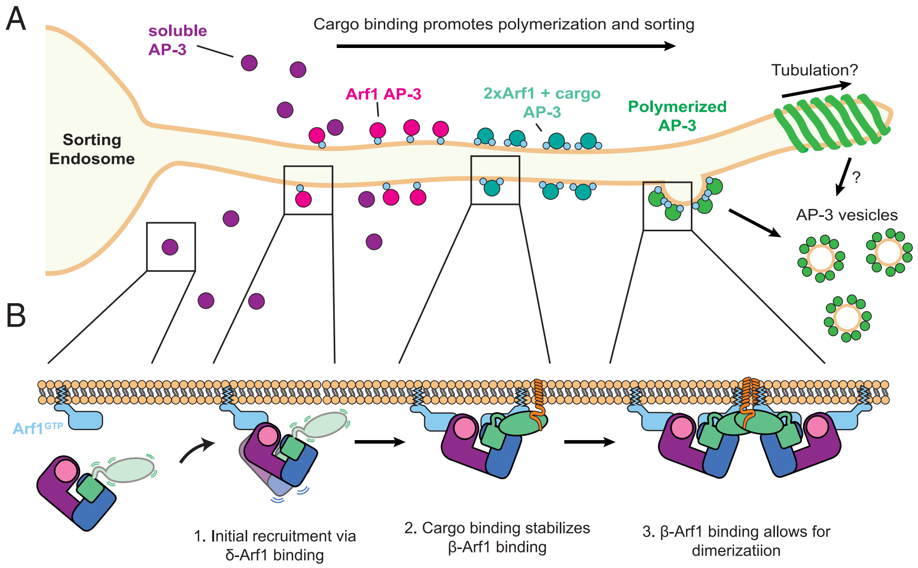

Fig. 6. Model for AP-3 membrane recruitment, cargo engagement, and coat assembly. (*A*) Schematic showing AP-3 recruitment to a sorting endosome and enrichment into AP-3 coated structures. Blue circles represent GTP-activated Arf1. (*B*) Step-wise recruitment and assembly of AP-3 based on the four cryo-EM structures from this work.

Furthermore, the β3–Arf1 binding site establishes the nascent interface for dimerization, suggesting a link between cargo capture and initial onset of coat polymerization.

Implications for AP-1 vs. AP-3 Mediated Transport. The mechanisms for formation of clathrin-coated vesicles by the AP-1 and AP-2 cargo adaptors are well studied. While these complexes share many similarities (tertiary structure, cargo-binding sites, clathrin binding), their respective regulatory networks are largely dictated by a requirement for Arf1 in the case of AP-1 and a comparatively large assortment of regulators in the case of AP-2 (51). However, deciphering the regulatory networks for AP-1 versus AP-3 is more challenging. Compared to AP-2, which has several dozen well-studied regulators that control its function during endocytosis, the interaction networks for AP-1 and AP-3 are sparse and largely rely on the function of Arf1 for activation. Our data show that while both complexes engage with Arf1 in a similar manner (i.e. conserved binding sites), Arf1 binding causes distinct structural changes in AP-3 compared to AP-1. As Arf1 is actively engaged in forming contacts within AP-1 tubules (29), and our data show an Arf1–Arf1 dimer in the case of AP-3, it is likely that AP-3 can form higher-order assemblies. However, changes in the AP-3 vs. AP-1 backbone place the Arf1 molecules in distinct locations, implying that the ultrastructure of the AP-3 coat will be unique from those observed in AP-1. Further studies are required to elucidate whether AP-3 has the ability to form higher-order polymers and how the ultrastructure of these assemblies differs from AP-1 and COPI.

Activation, Cargo Binding, and Coat Assembly. A primary goal of vesicle coat assembly is to transport cargo between membrane-bound compartments. Much work has been done to decipher the molecular determinants of cargo binding, including the linear motifs that encode coat specificity (52) and the overall structure of the active, cargo-bound complexes. Much less is known about how, or if, cargo binding provides larger cues for complex regulation or coat assembly. Our structural data suggest, that at least in the case of AP-3, cargo binding drives distinct structural changes that have implications for coat assembly and a potential cross-talk between cargo binding sites. While β3 packing into the dileucine binding pocket was not observed in the soluble AP-3 structure (Fig. 1), it is observed in the presence of tyrosine cargo (Fig. 3). Whether tyrosine cargo binding will therefore compete with dileucine cargo binding, or if AP-3 can bind both cargo simultaneously, is unknown. Furthermore, it remains to be seen whether the membrane and cargo-bound AP-3 complex we observe is fully activated, or if intramolecular binding to the dileucine binding site represents a partially activated state. The effect on full activation of binding to a hypercurved membrane, as observed in our nanodisc structures, is also unclear. Further analysis using dileucine cargo on membranes of more physiological curvature will be required to understand the full activation pathway of AP-3.

Implications for Clathrin-Independent Vs. Clathrin-Dependent Roles of AP-3. While AP-3 has been reported to act in a clathrin-dependent (21) and independent manner (23, 53), whether these functions follow the mechanistic paradigms observed for AP-1 and AP-2 is an open question. AP-3 has a clathrin-binding motif in the β3 linker (22) and partially colocalizes with clathrin in vivo, although clathrin knockdown or inhibition does not fully disrupt traffic of AP-3-dependent cargoes (25). However, interaction with clathrin will likely have a strong effect on coat polymerization. Clathrin forms a rigid lattice of pentamers and hexamers. Whereas AP-2 has no higher-order assembly in AP-2/clathrin coats, it has been suggested that AP-1 can form assemblies that mirror the clathrin lattice (29, 54). However, AP-1 has also been reported to form tubules, which are not compatible with a clathrin lattice, suggesting they represent a clathrin-independent state of assembly.

While it is still unknown whether AP-3 can form tubular coats akin to AP-1, our findings that AP-3 contains multiple AH domains and can co-opt Arf1 for homodimerization suggests that a clathrin-independent tubular coat for AP-3 is likely. It is important to note that the conformation of the $\text{AP-3}^{\beta\text{-dimer}}$ we observe is not compatible with binding a flat membrane, as the spacing between the multiple membrane binding sites is too constricted (*SI Appendix*, Fig. S11). Major conformational rearrangements are certainly required to transition from a flat membrane assembly to what is observed in our nanodisc-bound $\text{AP-3}^{\beta\text{-dimer}}$. Whether these conformational changes are induced by membrane curvature or are required for curvature generation is unknown. However, the presence of two AH domains in AP-3 strongly implies that AP-3 can deform membranes, likely in a cooperative manner with Arf1, which is known to tubulate membranes (44).

Specificity in Arf1 Transport. While AP-1 and AP-3 share many commonalities in their overall reliance on Arf1 for membrane recruitment and activation, our data suggest that their initial interaction with Arf1 is distinct. Our data suggest that the primary Arf1 recruitment site on AP-3 is the δ subunit, in contrast to the β subunit for AP-1. Interestingly, in humans, AP-3 δ has only a single isoform (*AP3D1*), whereas β3 has several isoforms (*AP3B1, AP3B2*). This is the inverse for AP-1, which has a single β1 isoform (*AP1B1*), but two γ isoforms (*AP1G1, AP1G2*). It is notable that in our structural analysis, we do not observe fully activated complexes in the absence of cargo. Single-molecule tracking using yeast AP-3 showed that Arf1 and cargo had a cooperative effect on AP-3 recruitment to membranes, where individual components showed only modest recruitment in isolation (28). Our data provide a structural mechanism for this observation, whereby tyrosine cargo and membrane binding results in rigidification of the complex and stabilization of the second Arf1 binding site on β3. In addition to a multiplicity of binding sites, assembly and activation of the coat is therefore associated with a distinct set of structural changes.

Implications for AP-3 Regulation. Our structural analysis provides a stepwise mechanism for recruitment and activation of the AP-3 coat. How this core mechanism is further regulated and controlled is an open question. The δ appendage has been shown to have an autoinhibitory role on AP-3 recruitment via the δ-Arf1 interface (55). Furthermore, AP-3 is extensively posttranslationally modified, with a multitude of sites in the disordered linkers of the δ and β3 subunits (56). A full understanding of AP-3 function will therefore require a mechanistic dissection of how these multiple regulatory inputs influence AP-3 recruitment, cargo binding, and coat polymerization.

Materials and Methods

Full methods are available in *SI Appendix*.

Recombinant Protein Purification.

AP-3 complex purification. AP-3 core (δ 1-617; β3 residues 1 to 677; μ3; σ3) was coexpressed in *Escherichia coli* BL21 Star cells (Invitrogen) with HRV-cleavable glutahtion S-transferase tags on the C termini of δ and β3. Lysogeny broth (LB) cultures were induced in mid-log phase with 0.5 mM Isopropyl β-d-1-thiogalactopyranoside (IPTG) at 18 °C for 18 h. AP-3 was purified using batch binding to glutathione resin (GoldBio) and size-exclusion chromatography on a Superdex 200 Increase column (Cytiva).

Myristoylated Arf1 purification. Full-length human Arf1 (Q71L) was coexpressed in BL21 (DE3) *E. coli* with plasmids encoding human myristoyltransferase 1 and *E. coli* methionylaminopeptidase. LB cultures were supplemented with 50 μM myristic acid 20 min prior to induction. Cultures were induced with 0.4 mM IPTG at 20 °C for 18 h. Arf1 was purified using batch binding to nickel-nitrilotriacetic acid (Ni-NTA) resin (GoldBio) and myristoylated Arf1 was separated from unmodified Arf1 using a Phenyl Sepharose HiTrap column (GE) and further purified on a Superdex 75 Increase column (Cytiva).

His-tagged purifications. Several constructs used in this study were purified as fusions to an N-terminal 10× polyhistidine fused with either a Halo tag, a small ubiquitin-like modifier tag, or both. For each, proteins were expressed in BL21 *E. coli* and purified via batch binding on Ni-NTA resin.

MSP2N2 purification. MSP2N2 was purified essentially as described (38). Briefly, MSP2N was expressed in BL21 (DE3) *E. coli* at 20 °C for 16 h with 0.5 mM IPTG. MSP2N was purified using batch binding to Ni-NTA resin and ion exchange chromatography using a HiTrap Q HP column (Cytiva).

In Vitro Pulldowns. Halo-tagged fusion proteins (200 pmol) were bound to 10 μL of Magne® HaloTag® Beads (20% slurry, Promega), followed by washing. Bound beads were incubated with 200 pmol of AP-3, incubated for 1 h, and eluted for 1 to 3 h with 100 pmol of HRV 3C protease. GDP conditions were performed with full-length Arf1 T31N and GTP conditions were performed with full-length Arf1 L8K, Q71L. GDP or GTP exchange was performed during the initial binding of Halo-Arf1 to the resin.

Membrane Binding Assays. SLBs were assembled from silica microspheres (Bangs Labs) and small unilamellar vesicles, essentially as described (57). Membranes contained a molar lipid ratio of 75% 1,2-dioleoyl-sn-glycero-3-phosphocholine (DOPC), 20% 1,2-dioleoyl-sn-glycero-3-phospho-L-serine (DOPS), and 5% 1,2-dioleoyl-sn-glycero-3-phospho-(1′-myo-inositol-3′-phosphate) (PI(3)P). SLBs were mixed with 1 nmol protein in 100 μL volume and washed with buffer containing 100 mM NaCl (low salt), 1 M NaCl (high salt), or 0.1% Triton X-100. To ensure the integrity of the membrane, SLBs were never aspirated into the pipette tip and pelleting was performed at 400 × *g*.

Nanodisc/Cargo/Arf1/AP-3 Assembly for Cryo-EM. Nanodiscs were assembled as in ref. 38, with MSP2N2 and a lipid ratio of 73 mol% DOPC: 20 mol% DOPS: 5 mol%PI3P: 2 mol% oleic acid-conjugated cargo peptide. Purified AP-3 core was incubated with LAMP1-containing nanodiscs for 1 h at 21 °C followed by addition of *myr*Arf1, GTP, *s*ARNO, and EDTA and gently inverted for an additional 25 mins before being quenched via addition of $MgCl_2$ to produce ~4 μM of assembled complex.

Cryo-EM Structure Determination.

Blot-free sample preparation. Self-wicking nanowire grids (1.2/0.8, 300 copper mesh; SPT Labtech) were backside coated with a layer of gold ~400 to 500 Å thick. Grids were glow discharged and plunge frozen using a chameleon® vitrification robot (SPT Labtech). Protein concentration was 7 μM for soluble AP-3 and 4 μM for AP-3/Arf1/nanodisc.

Data collection. Data were collected at the Simons Electron Microscopy Center at the New York Structural Biology Center (NYSBC) on a ThermoFisher Titan Krios equipped with a Gatan Imaging Filter. Microscope parameters are included in *SI Appendix*.

Data processing. Data processing was performed using cryoSPARC v4.4.1 (58). Movies were aligned using Patch Motion Correction, followed by Patch CTF Estimation. Datasets were manually curated to remove defocus and CTF fit outliers. For each dataset, particles were picked with Blob Picker, Template Picker, and crYOLO (59). Particles were extracted, and processed independently with extensive 2D classification. "Clean" particles, defined as those belonging to 2D classes with obvious internal structure and features representative of tertiary protein structure, were merged and duplicates removed.

Structure determination—Soluble AP-3. Clean particles (~2.7 million) were subjected to Non-Uniform (NU) refinement followed by 3D classification without alignment. A final subset of particles (~1.2 million particles) was subjected to NU refinement with a final nominal gold-standard Fourier shell correlation (GSFSC) resolution of 3.6 Å. This map was deposited into the Electron Microscopy Database (EMDB) under accession code EMD-45214.

Structure determination—LAMP1-nanodisc bound AP-3. ~1 million clean particles were 3D classified using ab initio model generation with three classes. This yielded classes corresponding to soluble AP3, AP-3 bound to a single Arf1 molecule (AP-3^{monoARF}), and a dimer of AP-3 (AP-$3^{\beta\text{-dimer}}$). The soluble AP-3 particles were discarded and the AP-3^{monoARF} and AP-$3^{\beta\text{-dimer}}$ subsets were further processed. The AP-3^{monoARF} particles were refined and then classified using 3D classification without alignment. This yielded a final dataset of 285,082 particles, which were refined using NU refinement to a final nominal GSFSC resolution of 4.6 Å. This map was deposited into the EMDB under accession code EMD-45207. The original AP-$3^{\beta\text{-dimer}}$ class was further processed to remove AP-3 "monomers." This yielded a subset of 122,155 particles with well-resolved density for both copies of AP-3 in a C1 refinement. These particles were subjected to NU refinement with C2 symmetry, leading to final map with a nominal GSFSC resolution of 4.3 Å (deposited under EMDB accession code EMD-45208). To better resolve the Arf1 homodimeric interface that mediates the AP-$3^{\beta\text{-dimer}}$, we performed a round of local refinement with C2 symmetry using a focus mask that encompassed Arf1, the N terminus of β3, and μ3. This led to map with a final GSFSC resolution of 4.2 Å (deposited under EMDB accession code EMD-45209). To determine a model of the "monomeric" AP-$3^{\text{ARF+cargo}}$, we used symmetry expansion and partial signal subtraction on all AP-$3^{\beta\text{-dimer}}$ particles to remove one copy of AP3 from the dimer. These monomers were combined with the AP-$3^{\text{ARF+cargo}}$ particles identified during the first stages of 3D classification and refined. Particles were further classified using 3D classification without alignment, which lead to a final refinement with a GSFSC resolution of 4.5 Å (deposited under EMDB accession code EMD-45210). To better resolve the interface with the membrane, two focused refinements were performed using masks that encompassed either the δ-Arf1 interface and a portion of the nanodisc density, or the β3-Arf1 interface and a portion of the nanodisc density. This led to focused refinement maps with an overall GSFSC resolution of 5.6 Å and 4.3 Å, respectively (deposited under EMDB accession codes EMD-45211 and EMD-45212). Combined half maps and full map were created using the phenix.combine_focused_maps feature and deposited under EMDB accession code EMD-45213.

Model Building and Validation. For each structure, an Alphafold model was predicted using sequences for human AP-3 core (δ 1-617; β3 residues 1-677; μ3; σ3), either with or without Arf1 and docked into the cryo-EM map. Model building and visualization was performed with a deepEMhancer (60) sharpened map and refinement was performed against a B-factor sharpened map. Models were refined using a multimodel approach in Rosetta (61) and ranked first by Rosetta Energy Score, followed by MolProbity (62) score. Final models were then further refined using Rosetta Relax, followed by B-factor refinement in Phenix (v1.21.1) (63). Certain regions of the initial AlphaFold models were rebuilt manually using Coot (64) before Rosetta analysis. A more detailed description of model building is included in *SI Appendix*.

Data, Materials, and Software Availability. Cryo-EM data are deposited in the EMDB under accession numbers EMD-45207 (65), EMD-45208 (66), EMD-45209 (67), EMD-45210 (68), EMD-45211 (69), EMD-45212 (70), EMD-45213 (71), and EMD-45214 (72). Associated atomic coordinates are deposited in the Protein Data Bank (PDB) under accession numbers 9C58 (73), 9C59 (74), 9C5A (75), 9C5B (76), 9C5C (77). Motion-corrected micrographs are deposited in the EMPIAR database (78) under accession numbers EMPIAR-12310 (79) for soluble AP-3 core and EMPIAR-12311 (80) for AP-3 core on a nanodisc. Plasmids/vectors for a subset of DNA constructs described in this work have been deposited with Addgene. Sequences for proteins encoded by these constructs are available in *SI Appendix*.

ACKNOWLEDGMENTS. We thank the laboratories of Drs. Gary Pielak, Brian Kuhlman, Richard Kahn, and James Hurley for their kind gifts of reagents. We thank the Dr. Chris Fromme laboratory and Dr. Leiah Carey for technical expertise and discussion. We thank Drs. Patrick Brennwald, Morgan DeSantis, and Frederick Hughson for helpful comments. We acknowledge Dr. Joshua Strauss of the University of North Carolina at Chapel Hill (UNC) Cryo-EM Core Facility, which is supported in part by National Cancer Institute (NCI) grant P30CA016086 as part of the UNC Center for Structural Biology. We acknowledge Dr. Laura Herring of the UNC Proteomics Core Facility, which is supported in part by NCI Center Core Support Grant (2P30CA016086-45) to the UNC Lineberger Comprehensive Cancer Center. Some of this work was performed at the National Center for Cryo-EM Access and Training and the Simons Electron Microscopy Center located at the New York Structural Biology Center, supported by the NIH Common Fund Transformative High Resolution Cryo-Electron Microscopy program (U24 GM129539), and by grants from the Simons Foundation (SF349247) and New York State Assembly. This work was supported by NIH-R35GM150960 (RWB) and by Alfred P. Sloan Foundation grant G-2021-14197 (RWB).

Author affiliations: [a]Department of Biochemistry and Biophysics, University of North Carolina at Chapel Hill School of Medicine, Chapel Hill, NC 27599; [b]Simons Electron Microscopy Center, New York Structural Biology Center, New York, NY 10027; and [c]Lineberger Comprehensive Cancer Center, University of North Carolina at Chapel Hill School of Medicine, Chapel Hill, NC 27599

1. S. R. Elkin, A. M. Lakoduk, S. L. Schmid, Endocytic pathways and endosomal trafficking: A primer. *Wien. Med. Wochenschr.* **166**, 196–204 (2016).
2. P. J. Cullen, F. Steinberg, To degrade or not to degrade: Mechanisms and significance of endocytic recycling. *Nat. Rev. Mol. Cell Biol.* **19**, 679–696 (2018).
3. A. Sanger, J. Hirst, A. K. Davies, M. S. Robinson, Adaptor protein complexes and disease at a glance. *J. Cell Sci.* **132**, jcs222992 (2019).
4. C. D'Souza-Schorey, P. Chavrier, ARF proteins: Roles in membrane traffic and beyond. *Nat. Rev. Mol. Cell Biol.* **7**, 347–358 (2006).
5. A. C. Theos *et al.*, Functions of adaptor protein (AP)-3 and AP-1 in tyrosinase sorting from endosomes to melanosomes. *Mol. Biol. Cell* **16**, 5356–5372 (2005).
6. K. Schledzewski, H. Brinkmann, R. R. Mendel, Phylogenetic analysis of components of the eukaryotic vesicle transport system reveals a common origin of adaptor protein complexes 1, 2, and 3 and the F subcomplex of the coatomer COPI. *J. Mol. Evol.* **48**, 770–778 (1999).
7. J. Hirst *et al.*, Characterization of TSET, an ancient and widespread membrane trafficking complex. *Elife* **3**, e02866 (2014).
8. J. B. Dacks, M. S. Robinson, Outerwear through the ages: Evolutionary cell biology of vesicle coats. *Curr. Opin. Cell Biol.* **47**, 108–116 (2017).
9. G. M. Beacham, E. A. Partlow, G. Hollopeter, Conformational regulation of AP1 and AP2 clathrin adaptor complexes. *Traffic* **20**, 741–751 (2019).
10. E. E. Heldwein *et al.*, Crystal structure of the clathrin adaptor protein 1 core. *Proc. Natl. Acad. Sci. U.S.A.* **101**, 14108–14113 (2004).
11. B. M. Collins, A. J. McCoy, H. M. Kent, P. R. Evans, D. J. Owen, Molecular architecture and functional model of the endocytic AP2 complex. *Cell* **109**, 523–535 (2002).
12. G. A. Mardones *et al.*, Structural basis for the recognition of tyrosine-based sorting signals by the μ3A subunit of the AP-3 adaptor complex. *J. Biol. Chem.* **288**, 9563–9571 (2013).
13. D. J. Owen, P. R. Evans, A structural explanation for the recognition of tyrosine-based endocytotic signals. *Science* **282**, 1327–1332 (1998).
14. B. T. Kelly *et al.*, A structural explanation for the binding of endocytic dileucine motifs by the AP2 complex. *Nature* **456**, 976 (2008).
15. M. A. Stamnes, J. E. Rothman, The binding of AP-1 clathrin adaptor particles to Golgi membranes requires ADP-ribosylation factor, a small GTP-binding protein. *Cell* **73**, 999–1005 (1993).
16. L. M. Traub, J. A. Ostrom, S. Kornfeld, Biochemical dissection of AP-1 recruitment onto Golgi membranes. *J. Cell Biol.* **123**, 561–573 (1993).
17. T. Serafini *et al.*, ADP-ribosylation factor is a subunit of the coat of Golgi-derived COP-coated vesicles: A novel role for a GTP-binding protein. *Cell* **67**, 239–253 (1991).
18. X. Yu, M. Breitman, J. Goldberg, A structure-based mechanism for Arf1-dependent recruitment of coatomer to membranes. *Cell* **148**, 530–542 (2012).
19. S. O. Dodonova *et al.*, A structure of the COPI coat and the role of coat proteins in membrane vesicle assembly. *Science* **349**, 195–198 (2015).
20. K. A. Beck, J. H. Keen, Interaction of phosphoinositide cycle intermediates with the plasma membrane-associated clathrin assembly protein AP-2*. *J. Biol. Chem.* **266**, 4442–4447 (1991).
21. M. T. Drake, Y. Zhu, S. Kornfeld, The assembly of AP-3 adaptor complex-containing clathrin-coated vesicles on synthetic liposomes. *Mol. Biol. Cell* **11**, 3723–3736 (2000).
22. E. C. Dell'Angelica, J. Klumperman, W. Stoorvogel, J. S. Bonifacino, Association of the AP-3 adaptor complex with clathrin. *Science* **280**, 431–434 (1998).
23. F. Simpson *et al.*, A novel adaptor-related protein complex. *J. Cell Biol.* **133**, 749–760 (1996).
24. J. Schoppe *et al.*, AP-3 vesicle uncoating occurs after HOPS-dependent vacuole tethering. *EMBO J.* **39**, e105117 (2020).
25. S. A. Zlatic *et al.*, Chemical-genetic disruption of clathrin function spares adaptor complex 3-dependent endosome vesicle biogenesis. *Mol. Biol. Cell* **24**, 2378–2388 (2013).
26. A. Stockhammer *et al.*, Multi-functional ARF1 compartments serve as a hub for short-range cargo transfer to endosomes. bioXriv [Preprint] (2023). https://doi.org/10.1101/2023.10.27.564143 (Accessed 6 June 2024).
27. A. A. Peden *et al.*, Localization of the AP-3 adaptor complex defines a novel endosomal exit site for lysosomal membrane proteins. *J. Cell Biol.* **164**, 1065–1076 (2004).
28. J. Schoppe *et al.*, Flexible open conformation of the AP-3 complex explains its role in cargo recruitment at the Golgi. *J. Biol. Chem.* **297**, 101334 (2021).
29. R. M. Hooy, Y. Iwamoto, D. A. Tudorica, X. Ren, J. H. Hurley, Self-assembly and structure of a clathrin-independent AP-1: Arf1 tubular membrane coat. *Sci. Adv.* **8**, eadd3914 (2022).
30. X. Ren, G. G. Farías, B. J. Canagarajah, J. S. Bonifacino, J. H. Hurley, Structural basis for recruitment and activation of the AP-1 clathrin adaptor complex by Arf1. *Cell* **152**, 755–767 (2013).
31. I. Razinkov *et al.*, A new method for vitrifying samples for cryoEM. *J. Struct. Biol.* **195**, 190–198 (2016).
32. A. J. Noble *et al.*, Reducing effects of particle adsorption to the air-water interface in cryo-EM. *Nat. Methods* **15**, 793–795 (2018).
33. G. Hollopeter *et al.*, The membrane-associated proteins FCHo and SGIP are allosteric activators of the AP2 clathrin adaptor complex. *Elife* **3**, e03648 (2014).
34. M. N. Seaman, P. J. Sowerby, M. S. Robinson, Cytosolic and membrane-associated proteins involved in the recruitment of AP-1 adaptors onto the trans-Golgi network. *J. Biol. Chem.* **271**, 25446–25451 (1996).
35. C. E. Ooi, E. C. Dell'Angelica, J. S. Bonifacino, ADP-ribosylation factor 1 (ARF1) regulates recruitment of the AP-3 adaptor complex to membranes. *J. Cell Biol.* **142**, 391–402 (1998).
36. M. Boehm, R. C. Aguilar, J. S. Bonifacino, Functional and physical interactions of the adaptor protein complex AP-4 with ADP-ribosylation factors (ARFs). *EMBO J.* **20**, 6265–6276 (2001).
37. C. Austin, M. Boehm, S. A. Tooze, Site-specific cross-linking reveals a differential direct interaction of class 1, 2, and 3 ADP-ribosylation factors with adaptor protein complexes 1 and 3. *Biochemistry* **41**, 4669–4677 (2002).
38. K. S. Cannon, R. M. Sarsam, T. Tedamrongwanish, K. Zhang, R. W. Baker, Lipid nanodiscs as a template for high-resolution cryo-EM structures of peripheral membrane proteins. *J. Struct. Biol.* **215**, 107989 (2023).
39. Y. Zhang *et al.*, Myr-Arf1 conformational flexibility at the membrane surface sheds light on the interactions with ArfGAP ASAP1. *Nat. Commun.* **14**, 7570 (2023).
40. L. P. Jackson *et al.*, A large-scale conformational change couples membrane recruitment to cargo binding in the AP2 clathrin adaptor complex. *Cell* **141**, 1220–1229 (2010).
41. K. L. Morris *et al.*, HIV-1 Nefs are cargo-sensitive AP-1 trimerization switches in tetherin downregulation. *Cell* **174**, 659–671.e14 (2018).
42. Y. Liu *et al.*, Clathrin-associated AP-1 controls termination of STING signalling. *Nature* **610**, 761–767 (2022).
43. X. Pang *et al.*, Structural elucidation of how ARF small GTPases induce membrane tubulation for vesicle fission. bioRxiv [Preprint] (2023). https://doi.org/10.1101/2023.12.19.572083 (Accessed 20 May 2024).
44. R. Beck *et al.*, Membrane curvature induced by Arf1-GTP is essential for vesicle formation. *Proc. Natl. Acad. Sci. U.S.A.* **105**, 11731–11736 (2008).

45. R. Beck *et al.*, Coatomer and dimeric ADP ribosylation factor 1 promote distinct steps in membrane scission. *J. Cell Biol.* **194**, 765–777 (2011).
46. R. Gautier, D. Douguet, B. Antonny, G. Drin, HELIQUEST: A web server to screen sequences with specific alpha-helical properties. *Bioinforma. Oxf. Engl.* **24**, 2101–2102 (2008).
47. E. A. Partlow *et al.*, A structural mechanism for phosphorylation-dependent inactivation of the AP2 complex. *Elife* **8**, e50003 (2019).
48. K. S. Cannon, B. L. Woods, J. M. Crutchley, A. S. Gladfelter, An amphipathic helix enables septins to sense micrometer-scale membrane curvature. *J. Cell Biol.* **218**, 1128–1137 (2019).
49. M. Giménez-Andrés, A. Čopič, B. Antonny, The many faces of amphipathic helices. *Biomolecules* **8**, 45 (2018).
50. M. G. J. Ford *et al.*, Curvature of clathrin-coated pits driven by epsin. *Nature* **419**, 361–366 (2002).
51. G. H. H. Borner *et al.*, Multivariate proteomic profiling identifies novel accessory proteins of coated vesicles. *J. Cell Biol.* **197**, 141–160 (2012).
52. L. M. Traub, Tickets to ride: Selecting cargo for clathrin-regulated internalization. *Nat. Rev. Mol. Cell Biol.* **10**, 583–596 (2009).
53. L. S. Newman, M. O. McKeever, H. J. Okano, R. B. Darnell, Beta-NAP, a cerebellar degeneration antigen, is a neuron-specific vesicle coat protein. *Cell* **82**, 773–783 (1995).
54. Q.-T. Shen, X. Ren, R. Zhang, I.-H. Lee, J. H. Hurley, HIV-1 Nef hijacks clathrin coats by stabilizing AP-1:Arf1 polygons. *Science* **350**, aac5137 (2015).
55. S. Lefrançois, K. Janvier, M. Boehm, C. E. Ooi, J. S. Bonifacino, An ear-core interaction regulates the recruitment of the AP-3 complex to membranes. *Dev. Cell* **7**, 619–625 (2004).
56. C. Azevedo, A. Burton, E. Ruiz-Mateos, M. Marsh, A. Saiardi, Inositol pyrophosphate mediated pyrophosphorylation of AP3B1 regulates HIV-1 Gag release. *Proc. Natl. Acad. Sci. U.S.A.* **106**, 21161–21166 (2009).
57. E. A. Partlow, K. S. Cannon, G. Hollopeter, R. W. Baker, Structural basis of an endocytic checkpoint that primes the AP2 clathrin adaptor for cargo internalization. *Nat. Struct. Mol. Biol.* **29**, 339–347 (2022).
58. A. Punjani, J. L. Rubinstein, D. J. Fleet, M. A. Brubaker, cryoSPARC: Algorithms for rapid unsupervised cryo-EM structure determination. *Nat. Methods* **14**, 290–296 (2017).
59. T. Wagner *et al.*, SPHIRE-crYOLO is a fast and accurate fully automated particle picker for cryo-EM. *Commun. Biol.* **2**, 218 (2019).
60. R. Sanchez-Garcia *et al.*, DeepEMhancer: A deep learning solution for cryo-EM volume post-processing. *Commun. Biol.* **4**, 1–8 (2021).
61. R.Y.-R. Wang *et al.*, Automated structure refinement of macromolecular assemblies from cryo-EM maps using Rosetta. *Elife* **5**, e17219 (2016), https://elifesciences.org/articles/17219.
62. V. B. Chen *et al.*, MolProbity: All-atom structure validation for macromolecular crystallography. *Acta Crystallogr. D Biol. Crystallogr.* **66**, 12–21 (2010).
63. P. V. Afonine *et al.*, Real-space refinement in PHENIX for cryo-EM and crystallography. *Acta Crystallogr. Sect. Struct. Biol.* **74**, 531–544 (2018).
64. P. Emsley, K. Cowtan, Coot: Model-building tools for molecular graphics. *Acta Crystallogr. D Biol. Crystallogr.* **60**, 2126–2132 (2004).
65. R. W. Baker, M. Begley, AP-3 bound to myristoylated Arf1 (Q71L). Electron Microscopy Database. https://www.ebi.ac.uk/emdb/EMD-45207. Deposited 6 June 2024.
66. R. W. Baker, M. Begley, Human AP-3 dimer bound to myristoylated Arf1 (Q71L) and LAMP1 cargo on a lipid nanodisc. Electron Microscopy Database. https://www.ebi.ac.uk/emdb/EMD-45208. Deposited 6 June 2024.
67. R. W. Baker, M. Begley, AP-3 Arf1 dimeric interface, focused refinement. Electron Microscopy Database. https://www.ebi.ac.uk/emdb/EMD-45209. Deposited 6 June 2024.
68. R. W. Baker, M. Begley, AP-3 bound to myristoylated Arf1 and LAMPI on a lipid nanodisc; consensus refinement. Electron Microscopy Database. https://www.ebi.ac.uk/emdb/EMD-45210. Deposited 6 June 2024.
69. R. W. Baker, M. Begley, AP-3 bound to myristoylated Arf1 and LAMPI on a lipid nanodisc; focus refinement 1. Electron Microscopy Database. https://www.ebi.ac.uk/emdb/EMD-45211. Deposited 6 June 2024.
70. R. W. Baker, M. Begley, AP-3 bound to myristoylated Arf1 and LAMPI on a lipid nanodisc; focus refinement 2. Electron Microscopy Database. https://www.ebi.ac.uk/emdb/EMD-45212. Deposited 6 June 2024.
71. R. W. Baker, M. Begley, AP-3 bound to myristoylated Arf1 (Q71L) and LAMPI on a lipid nanodisc; combined map. Electron Microscopy Database. https://www.ebi.ac.uk/emdb/EMD-45213. Deposited 6 June 2024.
72. R. W. Baker, M. Begley, Structure of human adaptor protein complex AP-3 in the apo state. Electron Microscopy Database. https://www.ebi.ac.uk/emdb/EMD-45214. Deposited 6 June 2024.
73. R. W. Baker, AP-3 bound to myristoylated Arf1 (Q71L). Protein Data Bank. https://www.rcsb.org/structure/9C58. Deposited 6 June 2024.
74. R. W. Baker, Human AP-3 dimer bound to myristoylated Arf1 (Q71L) and LAMP1 cargo on a lipid nanodisc. Protein Data Bank. https://www.rcsb.org/structure/9C59. Deposited 6 June 2024.
75. R. W. Baker, AP-3 Arf1 dimeric interface, focused refinement. Protein Data Bank. https://www.rcsb.org/structure/9C5A. Deposited 6 June 2024.
76. R. W. Baker, M. Begley, AP-3 bound to myristoylated Arf1 (Q71L) and LAMPI on a lipid nanodisc; combined map. Protein Data Bank. https://www.rcsb.org/structure/9C5B. Deposited 6 June 2024.
77. R. W. Baker, M. Begley, Structure of human adaptor protein complex AP-3 in the apo state; combined map. Protein Data Bank. https://www.rcsb.org/structure/9C5C. Deposited 6 June 2024.
78. A. Iudin *et al.*, EMPIAR: The electron microscopy public image archive. *Nucleic Acids Res.* **51**, D1503–D1511 (2023).
79. R. W. Baker, M. Begley, Cryo electron micrographs of AP-3 core bound to Arf1 and LAMPI on a lipid nanodisc. Electron Microscopy Public Image Archive. https://www.ebi.ac.uk/empiar/EMPIAR-12310. Deposited 30 September 2024.
80. R. W. Baker, M. Begley, Cryo electron micrographs of soluble human AP-3 core. Electron Microscopy Public Image Archive. https://www.ebi.ac.uk/empiar/EMPIAR-12311. Deposited 30 September 2024.